

Distinct behavior of localized and delocalized carriers in anatase TiO₂ (001) during reaction with O₂

Chiara Bigi ^{1,2}, Zhenkun Tang,^{3,4} Gian Marco Pierantozzi,¹ Pasquale Orgiani ^{1,5}, Pranab Kumar Das,^{1,6} Jun Fujii,¹ Ivana Vobornik,¹ Tommaso Pincelli,¹ Alessandro Troglia,^{1,2} Tien-Lin Lee,⁷ Regina Ciano,¹ Goran Drazic,⁸ Alberto Verdini,¹ Anna Regoutz,⁹ Phil D. C. King ¹⁰, Deepnarayan Biswas,¹⁰ Giorgio Rossi,^{1,2} Giancarlo Panaccione ^{1,*} and Annabella Selloni ^{3,†}

¹*Istituto Officina dei Materiali (IOM)-CNR, Laboratorio TASC, in Area Science Park, S.S.14, Km 163.5, I-34149 Trieste, Italy*

²*Dipartimento di Fisica, University of Milano, Via Celoria 16, I-20133 Milano, Italy*

³*Department of Chemistry, Princeton University, Princeton, New Jersey 08544, USA*

⁴*Department of Physics, Hengyang Normal University, 16 Heng-Hua Road, Zhu-Hui District, Hengyang 421008, People's Republic of China*

⁵*CNR-SPIN, UOS Salerno, Via Giovanni Paolo II 132, 84084 Fisciano, Italy*

⁶*International Centre for Theoretical Physics (ICTP), I-34100 Trieste, Italy*

⁷*Diamond Light Source, Harwell Science and Innovation Campus, Didcot OX11 0DE, United Kingdom*

⁸*Department for Materials Chemistry, National Institute of Chemistry, Hajdrihova 19, SI-1001 Ljubljana, Slovenia*

⁹*Department of Materials, Imperial College London, South Kensington, London SW7 2AZ, United Kingdom*

¹⁰*SUPA, School of Physics and Astronomy, University of St. Andrews, St. Andrews KY16 9SS, United Kingdom*



(Received 30 September 2019; revised manuscript received 3 February 2020; accepted 10 February 2020; published 28 February 2020)

Two-dimensional (2D) metallic states induced by oxygen vacancies (V_O s) at oxide surfaces and interfaces provide opportunities for the development of advanced applications, but the ability to control the behavior of these states is still limited. We used angle resolved photoelectron spectroscopy combined with density-functional theory (DFT) to study the reactivity of V_O -induced states at the (001) surface of anatase TiO₂, where both 2D metallic and deeper lying in-gap states (IGs) are observed. The 2D and IG states exhibit remarkably different evolutions when the surface is exposed to molecular O₂: while IGs are almost completely quenched, the metallic states are only weakly affected. DFT calculations indeed show that the IGs originate from surface V_O s and remain localized at the surface, where they can promptly react with O₂. In contrast, the metallic states originate from subsurface vacancies whose migration to the surface for recombination with O₂ is kinetically hindered on anatase TiO₂ (001), thus making them much less sensitive to oxygen dosing.

DOI: [10.1103/PhysRevMaterials.4.025801](https://doi.org/10.1103/PhysRevMaterials.4.025801)

I. INTRODUCTION

Many functional properties of anatase TiO₂ of relevance, e.g., in photocatalysis, solar cells and sensors, are critically affected by the presence of excess electrons induced by intrinsic defects, dopants, or photoexcitation [1–7]. Understanding and controlling the behavior of excess electrons is thus essential for improving TiO₂s performance in existing applications and for developing new applications as well. In particular, the chemical doping arising from oxygen vacancies (V_O s) induces important changes in the electronic structure, such as the creation of in-gap (IG) defect states, the formation of depletion regions, and band bending [3,8]. Another noteworthy feature connected with V_O s is the presence, under photoirradiation, of electronic states with metallic d character (Ti3d) at the anatase (101) and (001) surfaces, generally termed two-dimensional electron gas (2DEG) states [9–13]. First observed at the LaAlO₃/SrTiO₃ (LAO/STO) interface [14], 2DEGs have been reported both in transition metal oxide (TMO), parent compounds (e.g., bare surfaces of SrTiO₃ and KTaO₃),

and in engineered heterostructures [15,16]. Nevertheless, a number of important aspects are not yet settled, such as the depth distribution of the oxygen vacancies acting as electron donors. Another critical issue is the behavior of 2DEG and localized IG defect states under reducing versus oxidizing conditions, notably to what extent and in what conditions it is possible to control the excess of V_O s created by photoirradiation [9,10,17].

Here we combine ultraviolet and x-ray-based electron spectroscopies and first-principles density-functional theory (DFT) calculations to clarify the role, the formation mechanism, and the possible control of defect states formed at the (001) surface of anatase TiO₂ [18–20]. *In situ* UHV growth of high quality epitaxial thin films obtained by pulsed laser deposition (PLD) allowed us to identify the types of defect states that either appear under photoirradiation or can be induced and tailored by means of controlled postgrowth treatment (UHV annealing). Angle-resolved photoelectron spectroscopy (ARPES) measurements confirm the existence of both localized and delocalized electronic states, while resonant photoemission spectroscopy (RESPEs) in the soft x-ray range identifies their character as Ti³⁺ and Ti⁴⁺, respectively. Spectral changes were monitored while molecular O₂ was steadily fluxed on the sample surface through a metallic

*giancarlo.panaccione@elettra.eu

†aselloni@princeton.edu

capillary [21–23]. Remarkably, the results reveal that 2DEG delocalized features are robust against oxygen exposure, while the localized IG states are suppressed. Comparison with DFT calculations provides evidence of a distinct depth dependence of defect states. The 2DEG originates from subsurface V_{Os} and resides in subsurface layers due to the attractive potential resulting from these V_{Os} . In contrast, the deeper lying IG states that are suppressed by O_2 originate from the surface V_{Os} . Our results also provide a consistent explanation of previous contrasting findings and suggest possible strategies for controlling the carrier concentration and transport at the surface of anatase.

II. EXPERIMENTAL AND COMPUTATIONAL METHODS

A. Growth

Anatase TiO_2 thin films were grown by PLD at a dedicated chamber located at the APE-IOM laboratory (NFFA facility, Trieste, Italy) [24]. Rutile TiO_2 single crystal was ablated using a KrF excimer pulsed laser source kept at about 2 J/cm^2 energy density, with a typical laser repetition rate of 3 Hz. The substrate was kept at 700°C growth temperature, while oxygen background pressure was set to 10^{-4} mbar. Annealed samples have been kept at the growth temperature for 10 min in UHV (PLD chamber base pressure is the range of 10^{-7} mbar). Anatase TiO_2 thin films were grown on (001)-oriented $LaAlO_3$ (LAO) substrates. Epitaxial strainless condition was verified for these films. All the samples presented in this paper are ~ 20 nm thick.

B. Transmission and scanning transmission electron microscopy

A Cs probe-corrected Jeol ARM 200 CF scanning transmission electron microscope with a cold-FEG electron source operated at 200 kV was used for high-resolution imaging of the samples. Electron energy loss spectroscopy (EELS) was performed using a Gatan DualEELS Quantum ER system and elemental chemical analyses were performed with a Centurio Jeol Energy Dispersive X-ray Spectroscopy (EDXS) system with 100 mm^2 SDD detector. Cross-sectional samples in the [010] zone axis suitable for transmission electron microscopy (TEM) / scanning transmission electron microscopy (STEM) analyses have been obtained by a conventional polishing technique followed by dimpling and ion milling.

C. Ultraviolet ARPES, soft x-ray ARPES, RESPES

The as-grown samples were directly transferred *in situ* to the ARPES end station installed on the low-energy branch of the APE beamline (APE-LE) at Elettra synchrotron (Trieste, Italy). Such a chamber is equipped with a Scienta DA30 hemispherical electron energy and momentum analyzer (30° angular acceptance), which allows us to map the electronic bands over the extended areas of the Brillouin zone (BZ) without rotating the sample. ARPES experiments were performed at a base pressure $\sim 10^{-10}$ mbar and with the samples kept at liquid nitrogen. Photon energy of 46 eV was used with the light incidence angle of 45° . All light polarization available at the beamline has been exploited (linear vertical, linear horizontal, circular right, and circular left). When not otherwise specified, the overall energy resolution was set to ~ 40 meV,

and the angular resolution was set to 0.2° (corresponding to $\sim 0.01\text{ \AA}^{-1}$ at 46 eV photon energy).

Soft x-ray ARPES, resonant photoemission (RESPES), and oxygen dosing were performed at I09 beamline at Diamond Light Source (Didcot, United Kingdom). The samples fabricated at the APE-IOM laboratory were transferred to the Soft X-Ray branch of I09 beamline 120 by means of a UHV suitcase. The surface's contamination was thus prevented throughout the whole experiment. Sample temperature was 90 K. To reduce the effects of higher order components coming from the beamline optics in the RESPES measurements, the monochromator has been tuned to obtain the best compromise between flux, resolution, and higher order rejection. Furthermore, the residual second-order contribution was subtracted in all spectra. The energy position of the Fermi energy (E_F) and the energy resolution have been estimated by measuring the Fermi edge of poly-Au foil in thermal and electric contacts with the sample. The overall energy resolution (analyzer + beamline) was kept below 250 meV for the entire photon energy range. Molecular oxygen was injected through a metallic capillary placed close to the sample surface (i.e., $\sim 1\text{--}2$ cm). The amount of oxygen has been monitored by means of a residual gas analyzer (RGA) available in the experimental chamber. Base pressure in the experimental chamber was 1×10^{-10} mbar, up to a maximum O_2 partial pressure of 4×10^{-9} mbar.

D. Computational details

DFT calculations for pristine and reduced anatase (001) were performed using the VIENNA AB INITIO SIMULATION PACKAGE (VASP) [25,26]. We used the projector augmented-wave (PAW) pseudopotentials to describe the electron-ion interactions and the Perdew-Burke-Ernzerhof (PBE) functional [27] within the generalized gradient approximation (GGA) to treat the exchange-correlation interaction between electrons. The energy cut-off for the expansion of the wavefunctions was set to 500 eV. Since GGA is affected by the self-interaction error that favors delocalized electronic states, selected calculations using the PBE+U method with $U = 3.9$ eV [28] were also carried out to check the robustness of the PBE solutions (note that U values in the range 2.5–4 eV are typically used to describe defect states in TiO_2 [29,30]). While predicting a more structured electronic charge distribution in comparison to pure PBE, these PBE+U calculations confirmed the delocalized character of the subsurface excess electron states at the anatase (001) surface [31], which was also reported in a previous PBE+U study [32].

We modeled the anatase TiO_2 (001)-(1 \times 4) surface using a repeated slab geometry. We considered slabs of eight TiO_2 layers with a (3 \times 4) surface supercell for calculations of defect formation energies to minimize interactions between defects in periodic replicas, and slabs of 12 TiO_2 layers with a (2 \times 4) surface supercell for calculations of the electronic structure and charge densities. The vacuum region between consecutive slabs was larger than 12 \AA and dipole corrections were added to remove the electric field in this region [33]. A $3 \times 2 \times 1$ Monkhorst-Pack mesh was used to sample the BZ. All atoms of the slab were relaxed except those in the two bottom layers, which were kept fixed at their bulk positions.

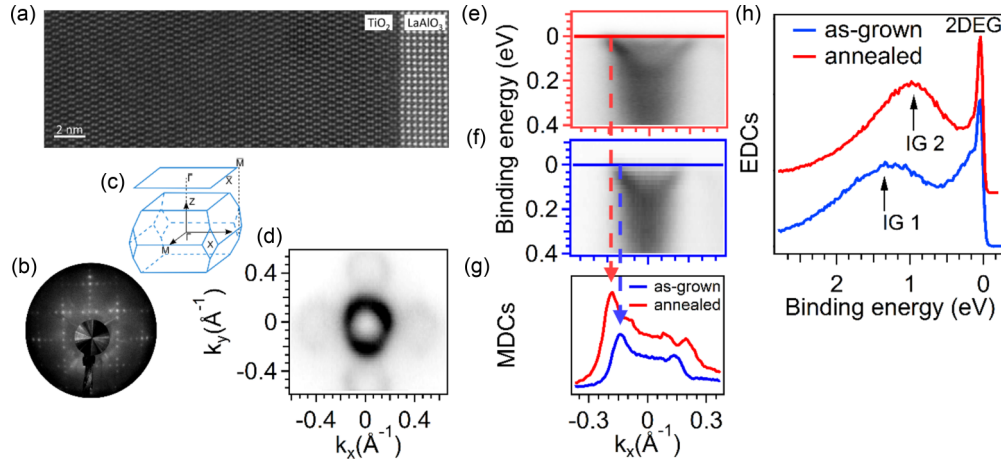


FIG. 1. (a) Representative high-resolution Z-contrast image of the TiO_2/LAO interfacial region. (b) LEED pattern (~ 110 eV) showing the $(1 \times 4) - (4 \times 1)$ surface reconstruction of the anatase thin films. (c) Sketch of the first BZ of anatase. (d) Fermi surface contour, measured at 46 eV photon energy, covering the first BZ, obtained by superimposing the Fermi surfaces measured with different light polarizations. (e), (f) ARPES spectra of the metallic state acquired at $h\nu = 46$ eV photon energy around the $\bar{\Gamma}$ point of the second Brillouin zone ($\bar{\Gamma}_1$): (e) 2DEG of anatase film with high amount of oxygen vacancies after the annealing treatment, (f) 2DEG of as-grown film. (g) MDCs at the Fermi level, in correspondence with the straight lines in panels (e) and (f) for the annealed (red) and as-grown (blue) samples, respectively; the dashed lines highlight the position of the Fermi momenta k_F . (h) EDCs extracted at the k_F of the outer band for the annealed (red) and the as-grown (blue) samples.

Geometry optimizations were carried out with convergence thresholds of 10^{-4} eV and 10^{-2} eV/ \AA for the total energy and the forces on the ions, respectively. Reaction pathways were determined using the climbing image nudged elastic band method [34].

Oxygen vacancies were created by removing a neutral oxygen atom. The resulting neutral V_O s consist of a vacant site, effectively bearing a 2+ positive charge, and two compensating excess electrons. Their formation energies were calculated as $E_{\text{form}}(V_O) = E_{\text{def}} - E_{\text{stoich}} + 1/2E_{\text{tot}}(\text{O}_2)$, where E_{def} and E_{stoich} are the total energies of the reduced (defective) and stoichiometric (defect-free) slabs, respectively, and $E_{\text{tot}}(\text{O}_2)$ is the total energy of the O_2 molecule.

III. EXPERIMENTAL RESULTS

A. Structural and ultraviolet ARPES results

Epitaxial strainless anatase TiO_2 thin films were grown by PLD on LAO substrates. Details of the growth protocol and structural characterization by x-ray diffraction are given elsewhere [24]. The results of our cross-sectional high-resolution TEM and high-angle annular dark-field scanning TEM measurements are shown in Fig. 1. In Fig. 1(a), a representative high-resolution Z-contrast image shows an atomically sharp interface region. The typical dumbbell structure of Ti ions in TiO_2 anatase is clearly distinguishable in the film and occurs in the entire film region with no sign of presence of secondary phases. The crystal quality of the films extends up to the surface, as confirmed by the low-energy electron diffraction (LEED) $(1 \times 4) - (4 \times 1)$ surface reconstruction pattern in Fig. 1(b) [9,10,24].

ARPES measurements were performed along the $\bar{\Gamma}-\bar{X}$ direction of the surface-projected BZ [Fig. 1(c)], obtained by superimposing the Fermi surfaces measured with different light polarizations (i.e., linear horizontal and vertical,

circular right and left). With such a procedure, we could compensate for the lack of intensity due to symmetry-related selection rules typically occurring for bands of d_{xy} orbital character. The surface structural reconstruction is reflected in the Fermi surface measured in the first Brillouin zone, shown in Fig. 1(d) and the Supplemental Material [31]: The bright circle centered at the $\bar{\Gamma}$ point corresponds to a 2DEG, characterized by a parabolic dispersion [Figs. 1(e) and 1(f)] and a d_{xy} orbital character arising from $\text{Ti}3d$ states typical in TMOs [9,11,15,35]. In addition, several replicas occur along both k_x and k_y directions, arising from the periodic lateral perturbation induced by the surface $(1 \times 4) - (4 \times 1)$ reconstruction [11,20]. Figures 1(e) and 1(f) compare the E versus k dispersion of the 2DEG for UHV annealed and as-grown samples, respectively. Both the as-grown and reduced samples were transferred *in situ* in UHV (i.e., without exposure to air) for the ARPES experiments. Two dispersive paraboliclike states are evident in Fig. 1(e): an outer parabola and a second (faint) quantized subband related to the confinement potential at the surface [11,12]. The bottom of the two quantized states is located at ~ 180 meV and ~ 65 meV for the outer and the inner bands, respectively, while the Fermi momenta (k_F) are at $\sim 0.18 \text{\AA}^{-1}$ and $\sim 0.11 \text{\AA}^{-1}$. These values are 25% larger than those obtained for the as-grown sample reported in Fig. 1(f). In addition, the bands of the annealed sample are located at ~ 45 meV higher binding energies. All these changes confirm electron doping of the sample due to the increase of V_O s by annealing, as observed elsewhere [30].

For a direct comparison between the Fermi wave vectors k_F of the annealed and as-grown samples, Fig 1(g) reports the momentum distribution curves (MDCs) at the Fermi energy E_F for the two films (red/blue lines in Figs. 1(e) and 1(f), respectively), while Fig. 1(h) shows the energy distribution curves (EDCs) obtained from Figs. 1(e) and 1(f) at the two different k_F vectors. In the latter, a broad intense

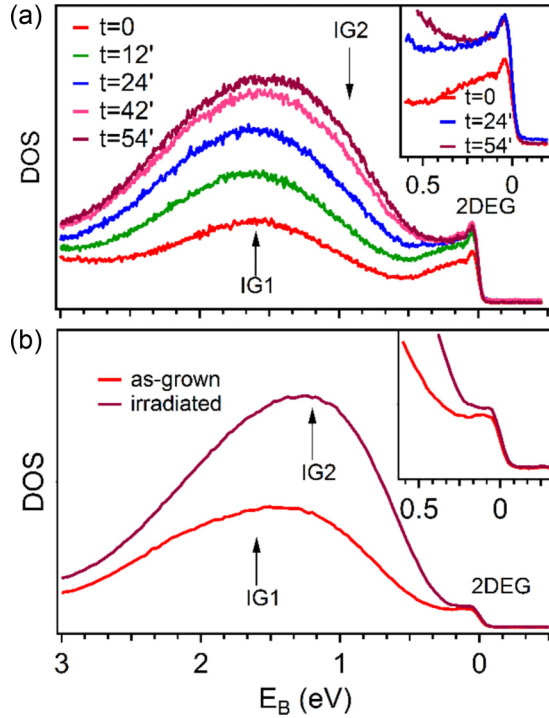


FIG. 2. DOS of anatase films deposited on LAO and measured at (a) APE beamline (Elettra, $h\nu = 46$ eV) in the highest beam flux condition available and (b) I09 beamline (Diamond Light Source, $h\nu = 120$ eV); in both panels, arrows indicate the position of the IGs for the as-grown and annealed samples, as discussed in the main text.

nondispersive state is found between ~ 1 eV and 2 eV of binding energy (BE), corresponding to localized IG states [13,22]. In the annealed samples, the spectral weight of IG states is shifted toward the Fermi energy; the asymmetric shape of the peak is consistent with the presence of a second IG state at lower BE (~ 1 eV). Such a state also appears upon beam irradiation and its spectroscopic intensity reaches a saturation value (see below). A further significant spectral change in the two EDCs of Fig. 1(h) is present at the Fermi energy: a shoulder on the 2DEG peak of the as-grown sample weakens after the annealing, consistently with an increased number of free carriers in the sample [9–12]. The electron carrier density values for the two samples are $n_{2D}^{\text{as-grown}} = 3 \times 10^{13}$ and $n_{2D}^{\text{annealed}} = 5 \times 10^{13} \text{ cm}^{-2}$ as calculated for two dimensional states with spin-degenerate bands [36].

The effects of intense beam irradiation on the electronic properties of oxide surfaces, including TiO_2 , have been investigated extensively [10,13,22,37,38]. Figure 2(a) reports the evolution of the spectral intensity versus time. The density of states (DOS) of the pristine surface (red curve, $t = 0$) displays IG states at ~ 1.6 eV BE. Under beam irradiation, the intensity of the DOS in the IG region increases and stabilizes after roughly 1 h of beam exposure. Similar to the IG states, the metallic 2DEG intensity also increases and saturates after about 25–30 min of beam irradiation. These findings agree with previous results [10,13], and are consistent with the evolution versus time observed at the Diamond Light Source. The asymmetric shape of the peak in both curves of Fig. 2(b) indicates the presence of at least a second, distinct, IG state.

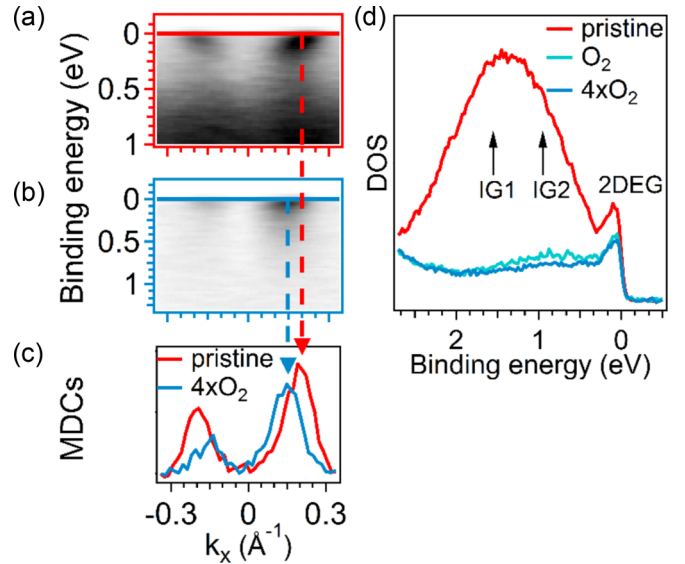


FIG. 3. ARPES spectra of a pristine as-grown (a) sample and (b) with molecular O_2 dosing. (c) MDCs extracted at E_F (red and light blue straight lines in panels (a) and (b), respectively, indicate where the MDCs have been extracted). (d) Evolution of the DOS upon oxygen dosing (red line corresponds to partial pressure $P = 1 \times 10^{-10}$ mbar, light blue $P = 1 \times 10^{-9}$ mbar and dark blue $P = 4 \times 10^{-9}$ mbar).

Similar to changes observed upon annealing, photoirradiation favors the formation of an IG located at shallower binding energies (i.e., ~ 1 eVBE). This may indicate that the localized states are related to two inequivalent oxygen vacancy sites and that the formation of the latter is more favorable under the beam.

B. Soft x-ray ARPES, resonant photoemission, and dosing experiment

While some reports suggest that the metallic state has a 3D character [9], a model linking the metallic state to the specific anatase surface arrangement has recently been shown to provide excellent agreement with the experimental data [11]. The 2D nature of the metallic state is also supported by experiments studying both the effect of electron doping through alkaline adsorption and the influence of beam irradiation at the anatase surface [10,12]. To gain further insight, we have performed soft x-ray ARPES and RESPES experiments, while simultaneously compensating the production of oxygen vacancies arising from photoirradiation. This has been achieved during the measurements by *in operando* fluxing molecular oxygen through a metal capillary positioned in the proximity of the sample surface [21–23]. Figure 3 shows the ARPES spectra acquired in the second BZ for the pristine sample in UHV (i.e., base pressure 1×10^{-10} mbar) measured with linearly polarized radiation of $h\nu = 120$ eV [Fig. 3(a)] and ARPES measured on the very same sample while dosing the surface with oxygen (i.e., base pressure 1×10^{-10} mbar; partial O_2 pressure 4×10^{-9} mbar) [Fig. 3(b)]. In Fig. 3(c), the MDCs extracted at E_F from Figs. 3(a) and 3(b) are compared.

The value of k_F is reduced from 0.19 \AA^{-1} to 0.15 \AA^{-1} ($\sim 20\%$) under oxygen dosing, i.e., it shows the opposite trend compared to that observed upon annealing in Figs. 1(e) and 1(f), giving direct evidence of (partial) healing of V_O s and consequent reduction of the number of free electron carriers at the surface, in agreement with previous reports [9]. Such a decrease corresponds to a reduction in the carrier density of $\sim 60\%$, qualitatively consistent with the theoretical picture for subsurface vacancies presented below. Figure 3(d) compares the angle-integrated DOS extracted from Figs. 3(a) and 3(b) with a BE range covering also the IG states. Almost complete suppression of the IG states is observed as soon as oxygen is dosed; the residual IG intensity is little affected by further increase of the oxygen partial pressure (four times the initial value), dropping below the background signal (it is visible only at resonance, see next section). Conversely, the 2DEG spectral weight is only slightly decreased and the reduction is mainly ascribable to the changes in the background signal. We also stress that the 2DEG maximum healing was already achieved at the lower oxygen partial pressure, as an increment of the oxygen pressure up to four times the initial dose (i.e., from 10^{-9} mbar to 4×10^{-9} mbar recorded on RGA) did not further affect the 2DEG state. Such a distinct behavior of IG and 2DEG has not been reported before in anatase TiO_2 .

In contrast to our results, studies on SrTiO_3 have shown that both the IG and the 2DEG are completely suppressed under O_2 dosing, with the spectral weights of the two states reducing at the same pace [15,17,22,38–40]. While incomplete compensation of the 2DEG was observed at the buried interface between a 4-u.c. epitaxial LaAlO_3 deposited on SrTiO_3 [22], in our study we are not sensitive to the film-substrate interface due to the short probing depth typical of photoemission spectroscopies. Therefore, our results should be compared to the bare SrTiO_3 rather than the LAO/STO buried interface.

The different reactivities of the IG and 2DEG in anatase suggest that these states may arise from different oxygen vacancy sites inside the material. Moreover, since the O_2 exposure in our setup occurs at the surface, the healing of the oxygen defects strongly depends on the V_O capability to migrate inside the material. The suppression of the IG suggests that the relative oxygen vacancies are located either at the surface or at buried sites that can easily move to the surface and recombine with the adsorbed molecules, as observed in anatase (101) [41]. Conversely, the 2DEG insensitivity against O_2 dosing indicates that the migration of the corresponding vacancies to the surface is unlikely, at least in the examined pressure and temperature range.

The electronic character of the 2DEG and the localized IG states was investigated by means of RESPEC measurements at the Ti $L_{2,3}$ edges. As both IG and 2DEG arise from $\text{Ti}3d$ states [11,12], RESPEC provides additional information by exploiting the energy shift between the core levels of titanium atoms with different oxidation states. Figure 4(a) shows the x-ray absorption spectra (XAS) measured in total electron yield (TEY) across the Ti L_3 edge from an as-grown sample (red curve) and under oxygen dosing (dark blue curve).

The four main peaks (located at approximate excitation energies of 458.3 eV, 460.5 eV, 463.5 eV, and 465.5 eV

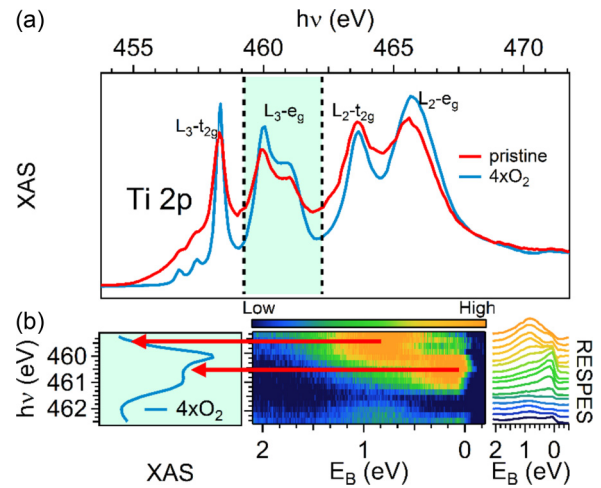


FIG. 4. (a) XAS spectra at Ti $L_{2,3}$ of a pristine (red) and during oxygen dosing (blue); (b) RESPEC in the second BZ upon oxygen dosing (color map—central panel—displays the momentum-integrated photoemission intensity; the resonant DOS curves show the different resonating energies for the IG and the 2DEG states (red arrows) are reported on the right).

excitation energies) can be ascribed to the combination of spin-orbit splitting of the initial states (L_3 - L_2) and crystal field splitting of the d orbitals in the final state (t_{2g} - e_g) for Ti atoms in 4+ oxidation state. The additional splitting of the L_{3-e_g} peak (~ 460.5 eV) is the fingerprint of the anatase phase arising from distortion of the ideal octahedron around Ti atom and long-range effects [42–44].

Effects of O_2 dosing on the absorption spectrum (total yield) edges of anatase TiO_2 film were measured at 90 K. The pristine sample refers to base pressure in the chamber of $[1 \times 10^{-10}]$ mbar, while the dark blue curve corresponds to the highest oxygen partial pressure of the present work (4×10^{-9} mbar). Upon oxygen dosing, the spectral intensity is lowered in the pre-edge as well as in the valleys at ~ 459 eV and ~ 462.5 eV, which correspond to spectral lines of Ti^{3+} [43]. As found in similar systems, e.g., rutile TiO_2 [45] and SrTiO_3 [46], the observed changes can be directly linked to the number of oxygen vacancies.

RESPEC in the second BZ were acquired upon oxygen dosing ($P = 1 \times 10^{-9}$ mbar). The angle-integrated photoemission EDCs, displayed as a color map in Fig. 4(b), indicate that the IG and 2DEG states resonate at different photon energies. The IG is peaked at an energy corresponding to a Ti^{3+} oxidation state, i.e., the valley at ~ 459.3 eV (roughly 0.8 eV away from the resonance of the 2DEG states), in agreement with previous results [22,24]. Conversely, the 2DEG follows the same trend of the XAS, with maximum intensity located around the L_{3-e_g} doublet at ~ 460.5 eV (characteristic of the stoichiometric Ti^{4+}). Similarly, above 462 eV (i.e., in the valley before the L_2 edge) the IG intensity rises first.

To better decouple the IGs and the 2DEG signals, we further investigated the DOS evolution at E_F as a function of the photon energy before and during oxygen dosing [Figs. 5(a) and 5(b)]. The IG states are strongly suppressed with oxygen dosing, yet both their BE and their resonating behavior are not

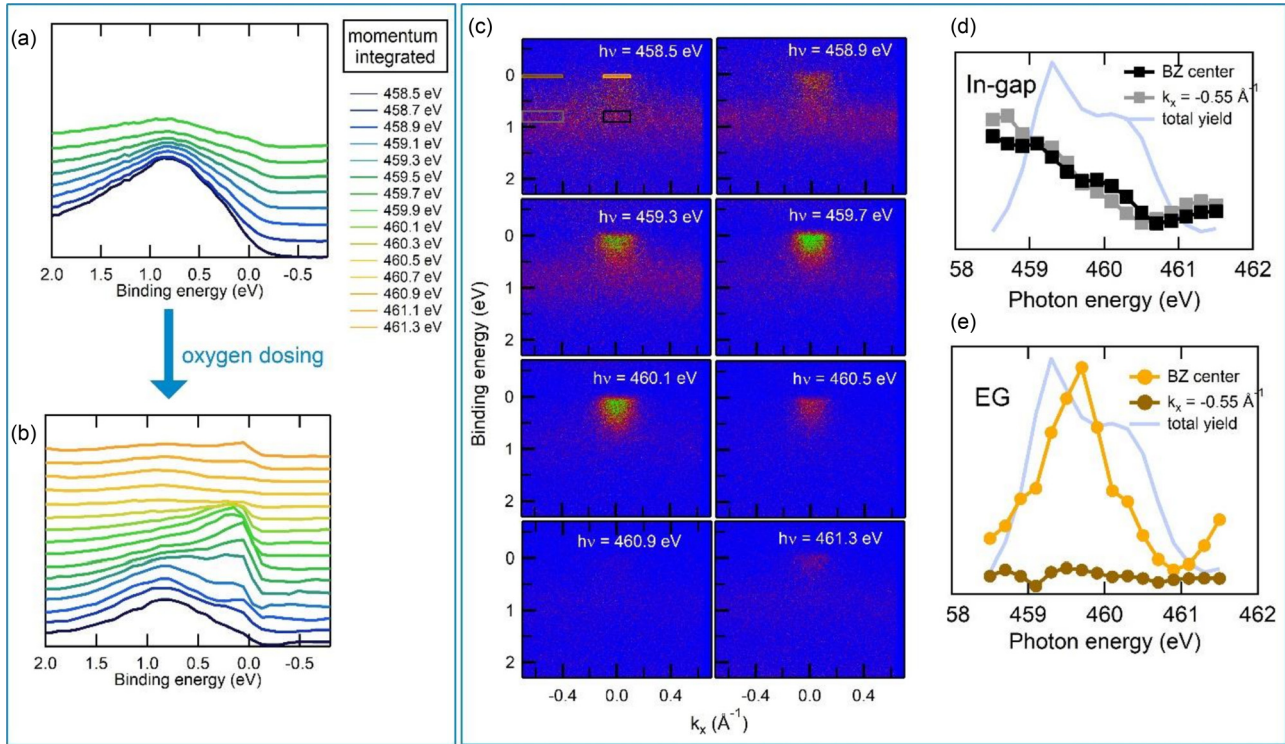


FIG. 5. (a), (b) DOS evolution at the Fermi level as a function of the photon energy before and during oxygen dosing. (c) Resonant angle-resolved-photoemission (RESARPES) spectra acquired while dosing oxygen. (d), (e) Intensity of the IG and 2DEG states across the Ti L_{3-e_g} absorption edge, respectively.

affected. The signal of the 2DEG is much clearer in Fig. 5(b), due to the strong suppression of the IG intensity upon oxygen dosing. RESARPES spectra, acquired in the 2BZ across the Ti L_{3-e_g} absorption edge while dosing oxygen at the surface, are shown in Fig. 5(c). The IG state is very visible as a nondispersive red broad line which resonates at the lowest photon energy (i.e., at 458.5 eV), whereas the electron pocket at Fermi is localized in the BZ center, more intense in the middle of the photon energy scan (459.7 eV). Figures 5(d) and 5(e) show the intensities of the IG and 2DEG states across the Ti L_{3-e_g} absorption edge. Each square (dot) in Fig. 5(d) [Fig. 5(e)] corresponds to ARPES spectra acquired at different photon energy. The colored rectangles in the top-left panel of Fig. 5(c) mark the BE/momentum region where the spectral intensity has been integrated. For both states, two regions of momentum space were selected: the projected 2BZ center ($\bar{\Gamma}_1$) and a low-symmetry momentum region. For the IG state, these correspond to the black and grey rectangles, respectively. Similarly, the spectral intensity at the Fermi level has been integrated in the same momentum ranges [i.e., center of 2BZ (orange) and outside (brown)]. The intensity of the IG state shows the same trend in both k regions, as expected for a localized state, while the 2DEG state disperses, having zero intensity outside the center (i.e., beyond 0.2 \AA^{-1} from $\bar{\Gamma}_1$). In both Figs. 5(d) and 5(e), the total electron yield acquired during the measurement is showed for comparison. As in the case of the angle integrated spectra, it appears that the 2DEG state resonates with the L_{3-e_g} doublet, whereas the IG state has Ti character, as it resonates on the rising edge of the $L_{3-t_{2g}}$ peak, out of the Ti^{4+} resonance.

Altogether, these findings provide evidence that (i) the 2DEG and the IG states could be related to distinct V_O sites and the former is robust against oxygen dosing, and (ii) the IGs are strongly localized on Ti atoms close to vacancy sites (Ti^{3+}) while the 2DEG wave function is delocalized over many Ti sites that largely maintain the Ti^{4+} oxidation state found in pristine TiO_2 .

C. Theoretical results

The observed different dependence of IG and 2DEG states to oxygen dosing suggests that they could be linked to different vacancy sites. To confirm this hypothesis, we performed DFT calculations of surface and subsurface V_O s at the anatase (001)-(1 \times 4) surface, with the underlying assumption that photoirradiation creates oxygen vacancies at the top few layers and vacancy diffusion to the bulk is negligible at the low temperature of our experiment [38]. We described the reconstructed surface using the widely accepted model of Ref. [20], where ridges exposing twofold coordinated oxygen (O_{2c}) and fourfold Ti atoms (Ti_{4c}) are separated by terraces exposing O_{2c} , threefold O (O_{3c}) and fivefold Ti (Ti_{5c}) atoms with a (1 \times 4) periodicity [Fig. 6(a)]. We used slabs of eight TiO_2 layers with a (3 \times 4) surface supercell to calculate V_O formation energies at the different surface and subsurface sites shown in Fig. 6(a).

From the computed V_O formation energies [Fig. 6(b)], it appears that oxygen vacancies are most likely to occur at surface VO1 (ridge O_{2c}) and VO4 (terrace O_{3c}) sites as well as at subsurface VO6 and VO7 sites, while the surface

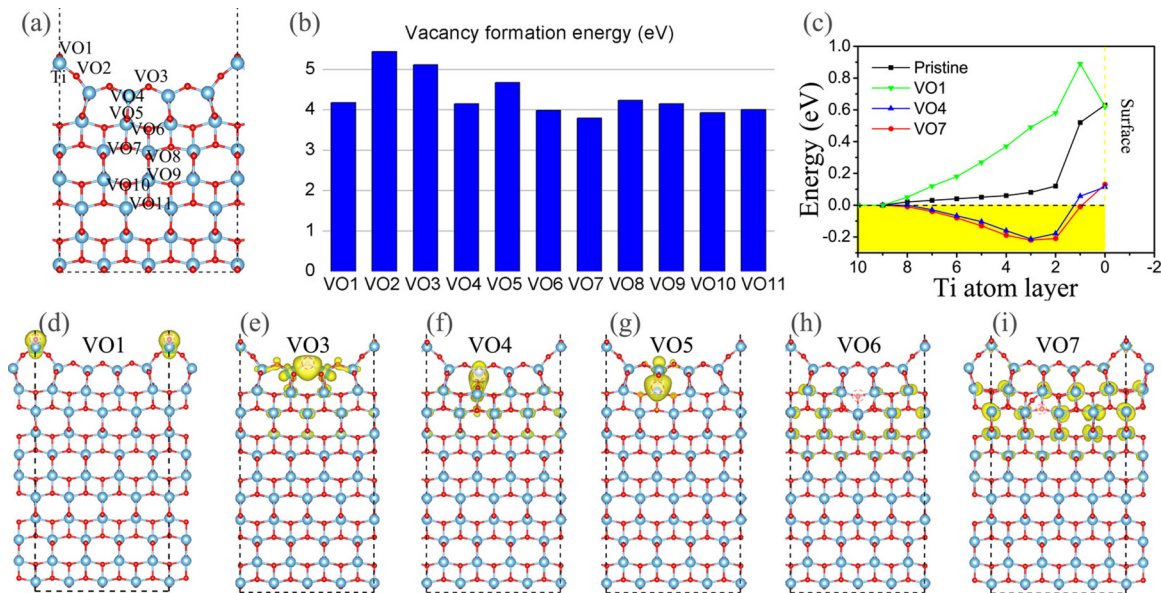


FIG. 6. (a) Side view of the reconstructed anatase $\text{TiO}_2(001)-1 \times 4$ slab model; the investigated oxygen vacancy sites are indicated; Ti and O atoms are light blue and red, respectively. (b) V_O formation energies (eV; blue bars) at different surface and subsurface oxygen sites computed using DFT-PBE; (c) Electrostatic potential profile in the surface region, computed from the shift of the Ti $3s$ peak in the different Ti layers of the pristine and reduced slabs with VO1, VO4, or VO7 defects. Here, layer 0 corresponds to the ridge Ti_{4c} sites, layer 1 to the terrace Ti_{5c} sites, and so forth. The yellow shading highlights the region of negative (attractive) potential; (d)–(i) Charge density contours of the excess electron states induced by VO1, VO3, VO4, VO5, VO6, and VO7, respectively; the vacancy positions are indicated by dashed red circles; dashed black lines show the unit cell used for the calculations. Additional density contours are shown in Supplemental Material [31].

VO2 and VO3 sites are energetically unfavorable. From the charge density plots in Figs. 6(d)–6(i) and the Supplemental Material [31], it also appears that the character of the defect states is very different for surface and subsurface V_O s, as these states become increasingly less localized moving from the surface to the subsurface. In particular, the two excess electrons from the vacancy are well localized on the Ti atoms adjacent to the vacant site and form deep energy levels in the band gap in the case of VO1, in agreement with previous calculations by Shi *et al.* [47]. In contrast, the defect states are partially delocalized in the case of VO4 and VO5 and become fully delocalized over few (001) planes in the case of subsurface VO6 and VO7 (and deeper V_O s as well), where they give rise to shallow energy levels at the bottom of the conduction band [31]. The delocalized character of subsurface defect states is confirmed by PBE+U calculations with $U=3.9$ eV, reported in the Supplemental Material [31].

The electrostatic potential profile in the surface region was computed from the energies of the semicore $\text{Ti}3s$ levels in different layers of the slab in the absence/presence of V_O s [31]. As shown in Fig. 6(c), the potential becomes repulsive near the surface of a defect-free slab [11,32], and this effect is further enhanced in the presence of VO1 (green line). In contrast, VO4 (blue) and VO7 (red) induce an attractive potential well of depth ~ 0.2 eV (very similar for VO4 and VO7) that confines the excess electron states in the subsurface Ti layers. Note that, unlike in previous modeling studies [11], this confining potential emerges naturally in our calculations for the reduced slabs.

To model the effect of oxygen dosing, we considered the adsorption of an O_2 molecule on the anatase surface with a

surface or subsurface V_O (Fig. 7). O_2 adsorption on TiO_2 is known to involve the transfer of excess electrons from the oxide to the molecule [1,3,41,48]. In the presence of a VO1, O_2 undergoes a strongly exothermic and barrierless adsorption at the vacancy site [31], which results in the formation of a bridging peroxide (O_2^{2-}) at the ridge, denoted (O_2)_o in Fig. 7. The two excess electrons of VO1 are both transferred to the adsorbed species, so no excess electron remains in TiO_2 , consistent with the strong reduction of the IG signal observed in ARPES when exposing the surface to O_2 .

A different picture holds for the adsorption of O_2 on a surface with subsurface V_O s. In this case, O_2 adsorbs at a terrace Ti_{5c} site and only one of the two excess electrons of the vacancy transfers to the molecule [1,3,48], thus resulting in the formation of an adsorbed superoxide (O_2^-), denoted O_2^* in Fig. 7. As previously discussed for the reaction of O_2 with the reduced anatase (101) surface [41], the negatively charged adsorbate has an attractive interaction with the subsurface vacancy, so migration of V_O toward the surface would be energetically favorable [Fig. 7(a)]. At variance with what was found for anatase (101) [41], however, the energy barrier for subsurface \rightarrow surface migration of the V_O is quite high at the anatase (001) surface [49], at least for the O_2 concentration considered here, as shown by Fig. 7(b) for the case of the VO4 \rightarrow VO3 migration step. It is thus quite likely that the V_O remains subsurface at the low temperature of our experiment, so the adsorbed O_2 remains a superoxide, i.e., one of the two excess electrons of the vacancy remains in TiO_2 . This explains the persistence of the 2DEG at the anatase- $\text{TiO}_2(001)$ as well as the decrease in the number of carriers observed under oxygen dosing without the necessity to include any interface effect with the substrate in the calculation.

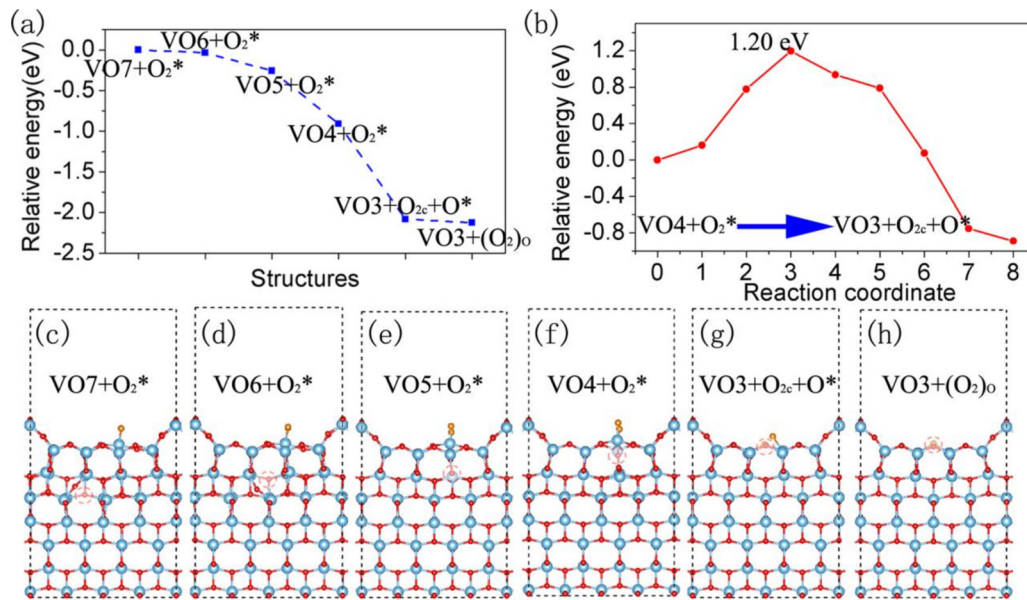


FIG. 7. (a) O_2 adsorption energy as a function of the subsurface (VO4–VO7) or surface (VO3) oxygen vacancy location. Relevant structures with a subsurface VO, denoted $VO_n+O_2^*$ ($n = 4 - 7$), are shown in panels (c)–(f). For VO3, two nearly degenerate structures are present, as shown in panels (g) and (h), where O^* indicates an oxygen adatom and $(O_2)_o$ a bridging peroxide replacing an O_{2c} . The energy zero corresponds to the adsorption energy of $VO_7+O_2^*$. (b) Energy barrier for the diffusion of an O vacancy from VO4 to VO3 in the presence of adsorbed oxygen. (c)–(h) Atomic geometries of adsorbed O_2 on reduced anatase (001) with a subsurface (VO4–VO7) or surface (VO3) oxygen vacancy, as described in (a). Ti atoms are blue, O atoms are red, adsorbed O_2 is orange; dashed red circles indicate the positions of the vacant sites.

IV. CONCLUSIONS

In summary, our results reveal distinct behaviors of localized and delocalized states induced by oxygen vacancies at the surface of anatase TiO_2 . Due to their different spatial locations and the kinetics of defect diffusion in anatase, the 2D delocalized states are much more robust than the localized IG states when exposed to molecular oxygen in a wide range of pressures. This robustness of the delocalized states is an important feature that could be exploited for different applications, e.g., to tune the electronic structure of TiO_2 in engineered interfaces and heterostructures or to precisely control the concentration of charge carriers in photosensitive devices.

Our findings unveil a relevant aspect of the surface chemistry of TiO_2 , providing a pathway to tailor the performance of future devices.

ACKNOWLEDGMENTS

This work has been partly performed in the framework of the Nanoscience Foundry and Fine Analysis (NFFA-MIUR

Italy) facility. We thank Fabio Miletto Granozio (Spin-CNR) and Ralph Claessen (Univ. Würzburg) for useful discussions. A.S. acknowledges the support of DoE-BES, Division of Chemical Sciences, Geosciences and Biosciences under Award No. DE-SC0007347. Z.T. was supported by the National Natural Science Foundation of China (No. 51602092), the Science and Technology Innovation Project Foundation of Hunan Province (No. 2018RS3103). G.D. acknowledges the financial support from Slovenian Research Agency (P2-0393). E. Cociancich from CNR-IOM and A. Di Cristoforo from Università Politecnica delle Marche are gratefully acknowledged for the support in the TEM specimen preparation.

G.P., C.B., P.O., and G.M.P. conceived the experiment(s), A.S. planned the computational studies. G.P., C.B., P.O., G.M.P., and A.S. wrote the paper with contributions from J.F., I.V., Z.T. All authors discussed the results, commented on the paper, and prepared written contributions. P.O. grew the films, G.D. and R.C. characterized samples. Z.T. performed the calculations. C.B., G.M.P., A.V., T.-L.L., A. R., P.D.C.K., G.R., A.T., T.P., D.B., and P.K.D., performed synchrotron radiation experiments and analyzed the data.

C.B. and G.M.P. contributed equally to this work.

- [1] T. L. Thompson and J. T. Yates, *Chem. Rev.* **106**, 4428 (2006).
 [2] A. Fujishima, X. Zhang, and D. A. Tryk, *Surf. Sci. Rep.* **63**, 515 (2008).

- [3] U. Diebold, *Surf. Sci. Rep.* **48**, 53 (2003).
 [4] C. Di Valentin, G. Pacchioni, A. Selloni, *J. Phys. Chem. C* **113**, 20543 (2009).

- [5] M. A. Henderson, *Surf. Sci. Rep.* **66**, 185 (2001).
- [6] S. X. Zhang, D. C. Kundaliya, W. Yu, S. Dhar, S. Y. Young, L. G. Salamanca-Riba, S. B. Ogale, R. D. Vispute, and T. Venkatesan, *J. Appl. Phys.* **102**, 013701 (2007).
- [7] J. Bai and B. Zhou, *Chem. Rev.* **114**, 10131 (2014).
- [8] A. G. Thomas, W. R. Flavell, A. K. Mallick, A. R. Kumarasinghe, D. Tsoutsou, N. Khan, C. Chatwin, S. Rayner, G. C. Smith, R. L. Stockbauer, S. Warren, T. K. Johal, S. Patel, D. Holland, A. Taleb, and F. Wiame, *Phys. Rev. B* **75**, 035105 (2007).
- [9] S. Moser, L. Moreschini, J. Jacimovic, O. S. Barisic, H. Berger, A. Magrez, Y. J. Chang, K. S. Kim, A. Bostwick, E. Rotenberg, L. Forro', and M. Grioni, *Phys. Rev. Lett.* **110**, 196403 (2013).
- [10] T. C. Rodel, F. Fortuna, F. Bertran, M. Gabay, M. J. Rozenberg, A. F. Santander-Syro, P. Le Fevre, *Phys. Rev. B* **92**, 041106(R) (2015).
- [11] Z. Wang, Z. Zhong, S. McKeown Walker, Z. Ristic, J. Z. Ma, F. Y. Bruno, S. Ricc , G. Sangiovanni, G. Eres, N. C. Plumb, L. Patthey, M. Shi, J. Mesot, F. Baumberger, and M. Radovic, *Nano Lett.* **17**, 2561 (2017).
- [12] R. Yukawa, M. Minohara, D. Shiga, M. Kitamura, T. Mitsuhashi, M. Kobayashi, K. Horiba, and H. Kumigashira, *Phys. Rev. B* **97**, 165428 (2018).
- [13] Y. Aiura, K. Ozawa, E. F. Schwier, K. Shimada, and K. Mase, *J. Phys. Chem. C* **122**, 19661 (2018).
- [14] A. Ohtomo and H. Y. Hwang, *Nature* **427**, 423 (2004).
- [15] A. F. Santander-Syro, O. Copie, T. Kondo, F. Fortuna, S. Pailhes, R. Weht, X. G. Qiu, F. Bertran, A. Nicolaou, A. Taleb-Ibrahimi, P. Le Fevre, G. Herranz, M. Bibes, N. Reyren, Y. Apertet, P. Lecoeur, A. Barthelemy, and M. J. Rozenberg, *Nature* **469**, 189 (2011).
- [16] P. D. C. King, R. H. He, T. Eknapakul, P. Buaphet, S. K. Mo, Y. Kaneko, S. Harashima, Y. Hikita, M. S. Bahramy, C. Bell, Z. Hussain, Y. Tokura, Z. X. Shen, H. Y. Hwang, F. Baumberger, and W. Meevasana, *Phys. Rev. Lett.* **108**, 117602 (2012).
- [17] W. Meevasana, P. D. C. King, R. H. He, S. K. Mo, M. Hashimoto, A. Tamai, P. Songsiririthgul, F. Baumberger, and Z. X. Shen, *Nat. Mater.* **10**, 114 (2011).
- [18] R. Hengerer, B. Bolliger, M. Erbudak, and M. Gratzel, *Surf. Sci.* **460**, 162 (2000).
- [19] G. S. Herman, M. R. Sievers, and Y. Gao, *Phys. Rev. Lett.* **84**, 3354 (2000).
- [20] M. Lazzeri and A. Selloni, *Phys. Rev. Lett.* **87**, 266105 (2001).
- [21] L. Dudy, M. Sing, P. Scheiderer, J. D. Denlinger, P. Schutz, J. Gabel, M. Buchwald, C. Schlueter, T.-L. Lee, and R. Claessen, *Adv. Mater.* **28**, 7443 (2016).
- [22] J. Gabel, M. Zapf, P. Scheiderer, P. Schutz, L. Dudy, M. St binger, C. Schlueter, T.-L. Lee, M. Sing, and R. Claessen, *Phys. Rev. B* **95**, 195109 (2017).
- [23] T.-L. Lee, D. A. Duncan, *Synch. Rad. News*, **31**, 16 (2018).
- [24] B. Gobaut, P. Orgiani, A. Sambri, E. Di Gennaro, C. Aruta, F. Borgatti, V. Lollobrigida, D. Ceolin, J.-P. Rueff, R. Ciancio, C. Bigi, P. K. Das, J. Fujii, D. Krizmancic, P. Torelli, I. Vobornik, G. Rossi, F. Miletto Granozio, U. Scotti di Uccio, G. Panaccione, *ACS Appl. Mater. Interfaces* **9**, 23099 (2017).
- [25] G. Kresse and J. Furthmuller, *Phys. Rev. B* **54**, 11169 (1996).
- [26] G. Kresse and J. Furthmuller, *Comput. Mater. Sci.* **6**, 15 (1996).
- [27] J. P. Perdew, K. Burke, M. Ernzerhof, *Phys. Rev. Lett.* **77**, 3865 (1996).
- [28] M. Setvin, C. Franchini, X. Hao, M. Schmid, A. Janotti, M. Kaltak, C. G. Van de Walle, G. Kresse, U. Diebold, *Phys. Rev. Lett.* **113**, 086402 (2014).
- [29] Z. Hu and H. Metiu, *J. Phys. Chem. C* **115**, 5841 (2011).
- [30] P. Scheiber, M. Fidler, O. Dulub, M. Schmid, U. Diebold, W. Hou, U. Aschauer, and A. Selloni, *Phys. Rev. Lett.* **109**, 136103 (2012).
- [31] See Supplemental Material at <http://link.aps.org/supplemental/10.1103/PhysRevMaterials.4.025801> for pictures of the Fermi surface as a function of light polarization, computed PBE band structure for pristine and reduced anatase (001)-(1 × 4), computed layer-resolved Ti-3s density of states, DFT+U calculations for reduced anatase, and potential energy profile for the adsorption of O₂ molecules at a VOI site.
- [32] S. Selcuk and A. Selloni, *Nat. Mater.* **15**, 1107 (2016).
- [33] L. Bengtsson, *Phys. Rev. B* **59**, 12301 (1999).
- [34] G. Henkelman, B. P. Uberuaga, and H. Jonsson, *J. Chem. Phys.* **113**, 9901 (2000).
- [35] P. D. C. King, S. McKeown Walker, A. Tamai, A. de la Torre, T. Eknapakul, P. Buaphet, S. K. Mo, W. Meevasana, M. S. Bahramy, and F. Baumberger, *Nat. Commun.* **5**, 3414 (2014).
- [36] J. M. Luttinger, *Phys. Rev.* **119**, 1153 (1960).
- [37] N. C. Plumb, M. Salluzzo, E. Razzoli, M. Månsson, M. Falub, J. Krempasky, C. E. Matt, J. Chang, M. Schulte, J. Braun, H. Ebert, J. Min r, B. Delley, K.-J. Zhou, T. Schmitt, M. Shi, J. Mesot, L. Patthey, and M. Radovi , *Phys. Rev. Lett.* **113**, 086801 (2014).
- [38] S. McKeown Walker, F. Y. Bruno, Z. Wang, A. de la Torre, S. Ricc , A. Tamai, T. K. Kim, M. Hoesch, M. Shi, M. S. Bahramy, P. D. C. King, and F. Baumberger, *Adv. Mater.* **27**, 3894 (2015).
- [39] C. Mathieu, S. Gonzalez, C. Lubin, O. Copie, V. Feyer, C. M. Schneider, and N. Barrett, *Surf. Interface Anal.* **51**, 7 (2019).
- [40] V. N. Strocov, A. Chikina, M. Caputo, M.-A. Husanu, F. Bisti, D. Bracher, T. Schmitt, F. Miletto Granozio, C. A. F. Vaz, and F. Lechermann, *Phys. Rev. Mater.* **3**, 106001 (2019).
- [41] M. Setvin, U. Aschauer, P. Scheiber, Y.-F. Li, W. Hou, M. Schmid, A. Selloni, and U. Diebold, *Science* **341**, 988 (2013).
- [42] P. Kruger, *Phys. Rev. B* **81**, 125121 (2010).
- [43] F. M. F. de Groot, M. O. Figueiredo, M. J. Basto, M. Abbate, H. Petersen, and J. C. Fuggle, *Phys. Chem. Minerals* **19**, 140 (1992).
- [44] S. O. Kucheyev, T. van Buuren, T. F. Baumann, J. H. Satcher, T. M. Willey, R. W. Meulenberg, T. E. Felner, J. F. Poco, S. A. Gammon, and L. J. Terminello, *Phys. Rev. B* **69**, 245102 (2004).
- [45] P. Le Fevre, J. Danger, H. Magnan, D. Chandesris, J. Jupille, S. Bourgeois, M. A. Arrio, R. Gotter, A. Verdini, and A. Morgante, *Phys. Rev. B* **69**, 155421 (2004).
- [46] C. Chen, J. Avila, E. Frantzeskakis, A. Levy, and M. C. Asensio, *Nat. Commun.* **6**, 8585 (2015).
- [47] Y. Shi, H. Sun, M. C. Nguyen, C. Wang, K. Ho, W. A. Saidi, and J. Zhao, *Nanoscale* **9**, 11553 (2017).
- [48] Y.-F. Li and A. Selloni, *J. Am. Chem. Soc.* **135**, 9195 (2013).
- [49] S. Selcuk, X. Zhao, and A. Selloni, *Nat. Mater.* **17**, 923 (2018).